

Intrinsic mechanism for anisotropic magnetoresistance and experimental confirmation in $\text{Co}_x\text{Fe}_{1-x}$ single-crystal films

F. L. Zeng,^{1,*} Z. Y. Ren,^{2,3,*} Y. Li,^{4,5} J. Y. Zeng,¹ M. W. Jia,¹ J. Miao,² A. Hoffmann,⁵ W. Zhang,^{4,5} Y. Z. Wu,^{1,6,†} and Z. Yuan^{3,‡}

¹*Department of Physics, State Key Laboratory of Surface Physics, Fudan University, Shanghai 200433, China*

²*School of Materials Science and Engineering, University of Science and Technology Beijing, Beijing 100083, China*

³*Center for Advanced Quantum Studies and Department of Physics, Beijing Normal University, Beijing 100875, China*

⁴*Department of Physics, Oakland University, Rochester MI 48309, USA*

⁵*Materials Science Division, Argonne National Laboratory, Lemont IL 60439, USA*

⁶*Collaborative Innovation Center of Advanced Microstructures, Nanjing 210093, China*

(Dated: January 20, 2022)

Using first-principles transport calculations, we predict that the anisotropic magnetoresistance (AMR) of single-crystal $\text{Co}_x\text{Fe}_{1-x}$ alloys is strongly dependent on the current orientation and alloy concentration. An intrinsic mechanism for AMR is found to arise from the band crossing due to magnetization-dependent symmetry protection. These special k -points can be shifted towards or away from the Fermi energy by varying the alloy composition and hence the exchange splitting, thus allowing AMR tunability. The prediction is confirmed by delicate transport measurements, which further reveal a reciprocal relationship of the longitudinal and transverse resistivities along different crystal axes.

The spin-dependent transport properties of magnetic materials are the basis of spintronics devices used, for example, for magnetic sensing and data storage [1]. The electrical conductance of a magnetic device usually depends on its magnetization configuration, resulting in so-called magnetoresistance (MR) effects. Among these effects, AMR [2–5] is fundamental for magnetic materials. It describes the dependence of the longitudinal electrical resistivity on the magnetization direction relative to the electric current in ferromagnetic materials.

AMR arises from the relativistic spin-orbit interaction (SOI), which couples the orbital motion of electrons with their spin angular momentum. The SOI leads to other spin transport phenomena, such as the anomalous Hall effect [6] and spin Hall effect [7], whose microscopic mechanisms have been extensively studied experimentally and theoretically. The extrinsic contributions due to impurity scattering, including skew scattering and side jump, have been identified, as has the intrinsic mechanism that results from the Berry curvature [8] of the energy bands. In contrast, the microscopic understanding of AMR is still unsatisfactory after a long history of study, especially in single-crystal materials [9–18]. Phenomenologically, AMR can be described by a conductivity tensor, which is a function of the magnetization and current directions with respect to the crystallographic axes [2, 3]. Alternatively, a two-current conduction model can be used to understand AMR, in which experimental values are usually needed to determine spin mixing parameters [5].

Recently, many SOI-driven MRs have been discovered, including spin-Hall [19], Rashba [20], and spin-orbital MRs [21], which also result in renewed interest in AMR, as it is a basic SOI-induced MR. Based on impurity scattering, some microscopic mechanisms for AMR have

been identified, where the free-electron-like conduction bands were usually applied [22]. Nevertheless, the intrinsic band-structure effect on AMR that is fundamental in physics and applicable to pure ferromagnetic metals is not yet clear. The lack of a comprehensive understanding of AMR further hampers its manipulation and application in spintronics devices.

In this Letter, we take a single-crystalline $\text{Co}_x\text{Fe}_{1-x}$ alloy as an example and perform a joint experimental and theoretical study of its AMR effect. The CoFe alloy simultaneously has a large magnetization and very low damping [23, 24] with strong anisotropy [25], making it already an important material in industry. The calculated AMR exhibits a strong dependence on the current direction, and its amplitude is larger in the alloy regime than in the pure-metal limits. Detailed analysis reveals that the special k -points near Fermi energy play an essential role, where energy bands form crossing and anti-crossing depending on the magnetization direction. This suggests an “intrinsic” mechanism for AMR arising from the band structure in addition to the “extrinsic” mechanisms based on the impurity-scattering picture. The predicted AMR properties are quantitatively confirmed by our transport experiments. A reciprocal relationship of the longitudinal and transverse resistivity is obtained along the $\langle 110 \rangle$ and $\langle 100 \rangle$ crystal axes.

AMR from first principles.—The resistivity ρ_{xx} of single-crystal $\text{Co}_x\text{Fe}_{1-x}$ alloy is calculated using the first-principles Landauer-Büttiker formalism including the SOI [26, 27]. For \mathbf{J} along $[100]$, we use a Cartesian coordinate system with $x \parallel [100]$, $y \parallel [010]$ and $z \parallel [001]$. Then, the calculated ρ_{xx} of $\text{Co}_{0.5}\text{Fe}_{0.5}$ is plotted in Fig. 1(c) as a function of the \mathbf{M} direction, where the angles α , β and γ are explicitly defined in Fig. 1(b). As α or γ

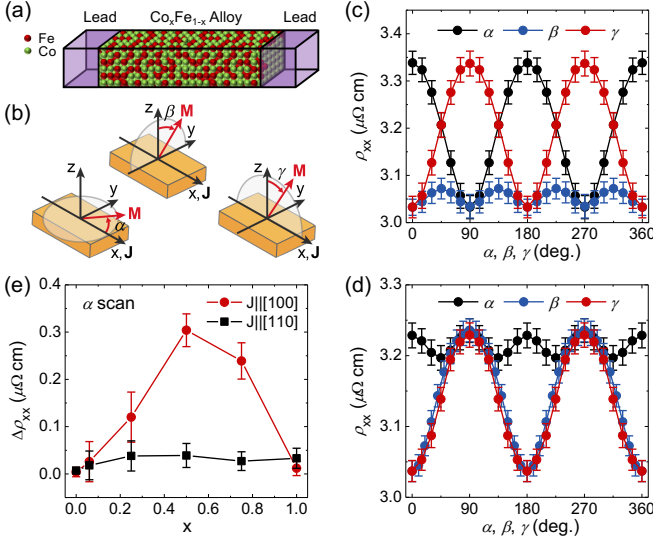


FIG. 1. (a) Sketch of the transport geometry in the calculation. (b) Definition of angles α , β and γ in Cartesian coordinates. The electric current \mathbf{J} is always along the x axis. Calculated ρ_{xx} of $\text{Co}_{0.5}\text{Fe}_{0.5}$ as a function of α , β and γ for $\mathbf{J} \parallel [100]$ (c) and $\mathbf{J} \parallel [110]$ (d). (e) Largest variation in $\Delta\rho_{xx}$ of the $\text{Co}_x\text{Fe}_{1-x}$ alloy when varying α as a function of Co concentration x .

varies, ρ_{xx} exhibits a two-fold symmetry, and the maximum (minimum) of ρ_{xx} occurs for $\mathbf{J} \parallel \mathbf{M}$ ($\mathbf{J} \perp \mathbf{M}$). A much weaker four-fold symmetry is found with varying β . The resistivity is shown in Fig. 1(d) for $\mathbf{J} \parallel x \parallel [110]$, $y \parallel [\bar{1}10]$, and $z \parallel [001]$, where $\rho_{xx}(\alpha)$ shows a weak four-fold symmetry, in sharp contrast to the case of $\mathbf{J} \parallel [100]$. The variations in ρ_{xx} are larger with rotation of β and γ , and both exhibit a two-fold symmetry. The calculated resistivity for $\mathbf{J} \parallel [110]$ shows an interesting relationship of $\rho_x \approx \rho_y > \rho_z$, which is in sharp contrast to the ordinary AMR relationship $\rho_x > \rho_y = \rho_z$ and has never been reported for any MRs.

We plot the largest variation in the resistivity $\Delta\rho_{xx} \equiv \max[\rho_{xx}(\alpha)] - \min[\rho_{xx}(\alpha)]$ in Fig. 1(e) as a function of Co concentration x . Here, a significant difference is seen for $\mathbf{J} \parallel [110]$ and $\mathbf{J} \parallel [100]$: $\Delta\rho_{xx}^{[110]}$ is at most $0.05 \mu\Omega \text{ cm}$ for all concentrations, while $\Delta\rho_{xx}^{[100]}$ is as large as $0.3 \mu\Omega \text{ cm}$ at $x = 0.5$. In addition, this giant current-orientation-dependent AMR is found to be more pronounced in alloys than in pure metals. This is counterintuitive because one would expect that the random arrangement of Co and Fe atoms in $\text{Co}_x\text{Fe}_{1-x}$ alloys would lower the crystalline symmetry of pure metals.

The intrinsic mechanism for AMR.—To understand the calculated AMR and unravel its microscopic nature, we focus on the electronic structure of bcc $\text{Co}_x\text{Fe}_{1-x}$ alloys. Applying the coherent potential approximation, we self-consistently compute auxiliary potentials for Co and Fe in $\text{Co}_x\text{Fe}_{1-x}$ alloys [28], and these effective potentials are randomly distributed in the transport calculations.

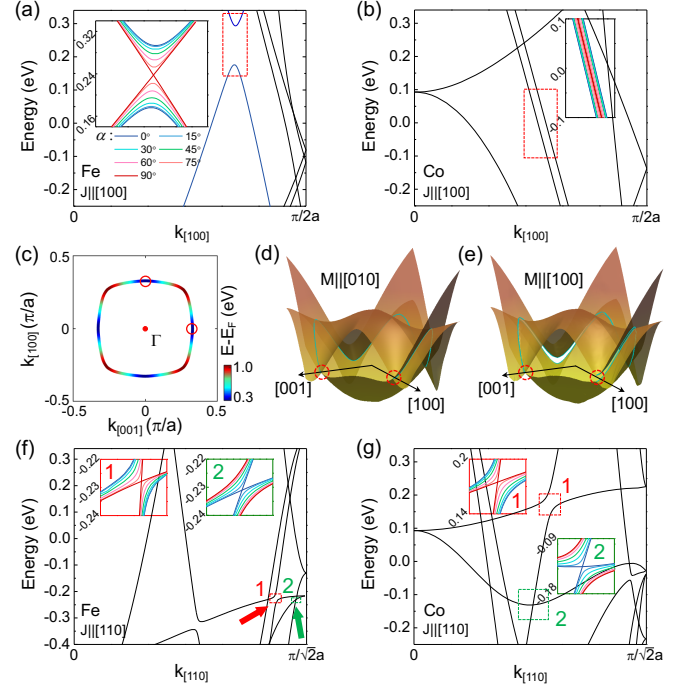


FIG. 2. Calculated band structure along [100] using the effective potentials of Fe (a) and Co (b) in $\text{Co}_{0.5}\text{Fe}_{0.5}$. (c) Nodal line in the (010) plane, to which the band crossing in (a) at $\alpha = 90^\circ$ belongs. Dispersion of the two bands forming the nodal line at $\alpha = 90^\circ$ (d) and $\alpha = 0^\circ$ (e). The nodal line disappears in (e), and an anticrossing band gap appears except for two special k -points along [001], as highlighted by red circles. Calculated band structure along [110] using the effective potentials of Fe (f) and Co (g) in $\text{Co}_{0.5}\text{Fe}_{0.5}$. In (a), (b), (f) and (g), only the bands marked by frames change with α , which are shown in the insets.

It is instructive to place the “effective Fe” potential on a perfect bcc lattice and non-self-consistently calculate the band structure [26]. Then, we perform the same calculation for bcc Co using the “effective Co” potential. These calculated band structures reflect the averaged electronic properties of Fe and Co atoms, whereas the bands are smeared in alloys due to the random arrangement of Fe and Co atoms.

The bands of Fe in $\text{Co}_{0.5}\text{Fe}_{0.5}$ along [100] for $\alpha = 0^\circ$ are plotted in Fig. 2(a), where a gap of $\sim 0.1 \text{ eV}$ appears near E_F , as highlighted by the red frame. When the magnetization rotates from $\alpha = 0^\circ$ to 90° , this gap shrinks until reaching a crossing point; see the inset. All the other bands along [100] near E_F do not depend on α . The crossing point at $\alpha = 90^\circ$ belongs to the nodal line located in the (010) plane with $\mathbf{M} \parallel [010]$, as shown in Fig. 2(c) and (d). This nodal line forms a closed ring around the Γ point and has the lowest energy close to E_F with the \mathbf{k} vector along $\langle 100 \rangle$, indicating its largest influence on the electronic transport for the current along $\langle 100 \rangle$. Since the magnetization breaks the time-reversal symmetry, this nodal line is protected by the mirror sym-

metry [29] about a crystalline plane perpendicular to \mathbf{M} . By rotating \mathbf{M} , the previous mirror symmetry is broken, and the nodal line disappears; see Fig. 2(e). Instead, an anticrossing gap appears except for at two special k -points along [001]. When \mathbf{M} is rotated to [100], another nodal line forms in the (100) plane. Therefore, the closing and opening of the band gap in Fig. 2(a) when rotating \mathbf{M} can be understood based on the required symmetry of the nodal line.

Around the crossing points, the two bands have different topological characteristics and do not interact with each other. Thus, the interband scattering has a relatively low probability. When the bands interact and form an anticrossing, the interband scattering rate increases such that the resistivity becomes larger [30–32]. From the quasi-particle point of view, the long effective wavelengths and small effective masses of the topological states have greater probabilities of surviving the back-scattering caused by disorder than other non-topological Bloch states [33, 34]. Therefore, ρ_{xx} in Fig. 1(c) monotonically decreases with increasing α and reaches the minimum at $\alpha = 90^\circ$. If we artificially shift E_F 0.2 eV upwards such that it approaches the crossing point, then the calculated $\Delta\rho_{xx}/\rho_{xx}$ increases by 12%. This numerical test confirms the correlation of the AMR and the \mathbf{M} -dependent band crossing [27]. Recently, the effect of the band topology on spin-dependent transport has been discussed in antiferromagnetic spintronics [35, 36].

Along [110], the Fe bands at two special k -points depend on the magnetization direction, which are marked by the frames with labels 1 and 2 in Fig. 2(f). At k -point 1, a gap appears at $\alpha = 0^\circ$ but closes at $\alpha = 90^\circ$. Conversely, the opposite α dependence occurs for the gap at k -point 2. The Co bands along [110] in Fig. 2(g) also have opposite α dependences at two k -points near E_F . The competing effects at these k pairs result in a non-monotonic variation in the resistivity for $\mathbf{J} \parallel [110]$ when α increases from 0° to 90° . Thus, the ordinary two-fold AMR is suppressed, and $\Delta\rho_{xx}^{[110]}$ is much smaller than $\Delta\rho_{xx}^{[100]}$. Disorder scattering in alloys breaks the momentum conservation, resulting in effective band broadening; therefore, the special k -points can affect the electrical resistivity, although they are not located precisely at the Fermi energy. Such band analysis is applicable in explanation of all the angular dependence shown in Fig. 1 [27].

The crossing points can be shifted up or down by varying the Co concentration x . When the crossing points move closer to E_F , their contribution to ρ_{xx} increases. For example, the band crossing in the Fe band along [100] gradually shifts down towards E_F with increasing x [27]; therefore, the AMR along [100] in Fig. 1(e) is more pronounced in the alloys than that in pure Fe. The calculated Co bands do not show significant variation for x up to 1, and the pure Co has a very small AMR, indicating that the band changes without gap closing and opening

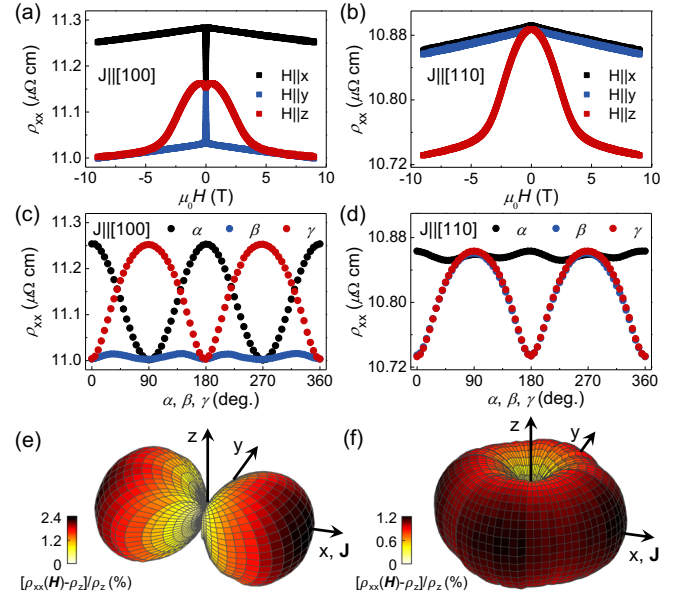


FIG. 3. Experimental resistivity along [100] (a) and [110] (b) of a 10-nm-thick $\text{Co}_{0.5}\text{Fe}_{0.5}$ sample measured under a magnetic field along principal axes x , y and z . The x axis is always defined as being along the current direction. Measured resistivity with rotating magnetization in the xy , yz and xz planes under the application of a 9-Tesla field with $\mathbf{J} \parallel [100]$ (c) and $\mathbf{J} \parallel [110]$ (d). The angles α , β and γ are defined in Fig. 1(b). Three-dimensional plots of the MR for the current along [100] (e) and [110] (f).

have little effect on the AMR.

We shall distinguish underlying physics for the quantities depending on the SOI-mediated band structure. The anomalous Hall effect results from Berry curvature at anticrossing bands, which contributes to the anomalous velocity [6, 8]. For Gilbert damping [26, 37–39] and magnetic inertia [40, 41], the SOI lifts bands across Fermi energy back and forth with rotating magnetization as described by the breathing Fermi surface model [42]. The intrinsic mechanism for AMR here comes from the symmetry protected topological states, which determines the dependence of longitudinal transport on crystal and magnetization directions.

Experimental measurements.—To verify the theoretical calculation and analysis, we performed AMR measurements on single-crystalline $\text{Co}_x\text{Fe}_{1-x}$ film deposited on $\text{MgO}(001)$ substrates by molecular beam epitaxy [27]. Figure 3(a) and (b) shows the measured resistivity of the $\text{Co}_{0.5}\text{Fe}_{0.5}$ film for $\mathbf{J} \parallel [100]$ and $\mathbf{J} \parallel [110]$, respectively, as a function of the external magnetic field, which is applied along the three principal axes. At a sufficiently large field, the measured ρ_{xx} linearly decreases with increasing field H , and this decrease can be attributed to the field-induced suppression of electron-magnon scattering [43].

We then performed transport measurements along

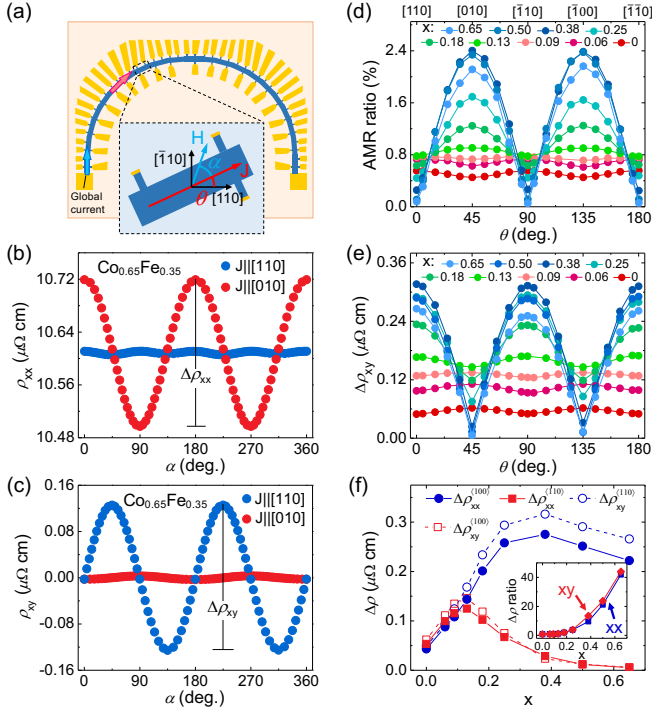


FIG. 4. (a) Schematic illustration of the device. The angle θ defines the current orientation direction with respect to $\text{Co}_x\text{Fe}_{1-x}[110]$. (b) ρ_{xx} and (c) ρ_{xy} measured on a 10-nm-thick $\text{Co}_{0.65}\text{Fe}_{0.35}$ alloy as a function of magnetic field direction for current along $[110]$ and $[010]$. Current-orientation-dependent AMR ratio (d) and $\Delta\rho_{xy}$ (e) for different Co concentrations x . (f) The current-orientation-dependent resistivity changes as a function of x . Inset: concentration-dependent ratios $\Delta\rho_{xx}^{(100)}/\Delta\rho_{xx}^{(110)}$ (blue) and $\Delta\rho_{xy}^{(110)}/\Delta\rho_{xy}^{(100)}$ (red).

$[100]$ and $[110]$ by rotating the applied 9-Tesla field in the xy , yz and xz planes, separately. As shown in Fig. 3(c), a strong two-fold symmetry of ρ_{xx} is seen as a function of α and γ for $\mathbf{J} \parallel [100]$, while a weak four-fold symmetry appears for the β scan. In contrast, for $\mathbf{J} \parallel [110]$, as shown in Fig. 3(d), a strong two-fold symmetry occurs in the β and γ scans, and a weak four-fold symmetry is obtained when varying α .

We then measured the MR under the field along an arbitrary direction by rotating the sample. The three-dimensional plots of the measured relative AMR, $[\rho_{xx}(\mathbf{H}) - \rho_z]/\rho_z$ with $\rho_z \equiv \rho_{xx}(H\hat{z})$, are shown in Fig. 3(e) and (f). The angular dependence shows a dumb-bell shape for $\mathbf{J} \parallel [100]$, which is expected for the AMR in most ferromagnetic materials. Nevertheless, the resistivity for $\mathbf{J} \parallel [110]$ exhibits a donut shape that has never been previously reported in literature and confirms the calculated relationship $\rho_x \approx \rho_y > \rho_z$. Note that the different angular-dependent AMRs in Fig. 3 are obtained with the same sample, indicating that the current-orientation effect arises from the electronic structure due to the anisotropic crystal field. The angular dependences of the resistivity measured in the experiment fully agree

with the calculated results in Fig. 1. Despite of the significant variation of ρ_{xx} with temperature and sample thickness, the quantitative agreement in the experimental and calculated $\Delta\rho_{xx}$ further confirms the predicted intrinsic nature [27]. At very small thickness, the emergence of interfacial spin-orbit field [16] may have additional effect on AMR, which is beyond the scope of this work.

We further developed our experiment to simultaneously measure the longitudinal and transverse resistivity under an arbitrary current orientation, as schematically shown in Fig. 4(a). The single-crystal $\text{Co}_x\text{Fe}_{1-x}$ films deposited on $\text{MgO}(001)$ substrates were patterned into $300 \mu\text{m} \times 100 \mu\text{m}$ Hall bars with continuously varying current directions. For $x = 0.65$, the experimental ρ_{xx} and ρ_{xy} are plotted in Fig. 4(b) and (c), which exhibit a reciprocal relationship. For $\mathbf{J} \parallel [010]$, the largest variation in longitudinal resistivity $\Delta\rho_{xx}$ is large when rotating \mathbf{H} , and the corresponding variation in transverse resistivity $\Delta\rho_{xy}$ is small. The opposite relationship of their amplitudes is found for $\mathbf{J} \parallel [110]$.

The measured AMR ratios defined by $\Delta\rho_{xx}/\min(\rho_{xx})$ and $\Delta\rho_{xy}$ with different Co concentrations are plotted in Fig. 4(d) and (e), respectively, both as a function of current orientation. Here, again, a reciprocal relationship between $\Delta\rho_{xx}$ and $\Delta\rho_{xy}$ is unambiguously demonstrated: at a given θ where $\Delta\rho_{xy}$ has its maximum amplitude, $\Delta\rho_{xx}$ has its minimum value, and vice versa. This reciprocal relationship is analytically reproduced [27] by the phenomenological expansion based on symmetry [44].

The AMR ratio exhibits a strong Co concentration dependence. At small x , the AMR ratio is nearly independent of the current direction θ , but for $x > 0.25$, a giant difference between the maximum at $\theta = 45^\circ$ and 135° and the minimum at $\theta = 0^\circ$ and 180° is observed. To quantitatively elucidate the concentration dependence, we plot $\Delta\rho_{xx}$ and $\Delta\rho_{xy}$ as a function of x in Fig. 4(f). For the current along $\langle 100 \rangle$, $\Delta\rho_{xx}$ increases with increasing x up to 0.38 and slightly decreases for larger x . In contrast, $\Delta\rho_{xx}^{(110)}$ has a relatively small amplitude. This current-orientation dependence and concentration dependence of $\Delta\rho_{xx}$ are both in very good agreement with the theoretical calculation in Fig. 1(e) except for the small bump at $x = 0.13$ in the red curves. This bump may be attributed to the inhomogeneity in the alloy samples at small x while homogeneous mixing is assumed in calculation. Moreover, the ratio between the experimental $\Delta\rho_{xx}^{(100)}$ and $\Delta\rho_{xx}^{(110)}$ monotonically increases with x and is as large as 42 at $x = 0.65$, as shown in the inset of Fig. 4(f). Such a large anisotropic dependence on the current orientation has never been previously reported for the AMR. Following the reciprocal relation, $\Delta\rho_{xy}^{(110)}/\Delta\rho_{xy}^{(100)}$ has the same dependence on x .

Conclusions.—We have calculated the AMR in single-crystal $\text{Co}_x\text{Fe}_{1-x}$ alloys using a first-principles transport

formalism. Our band structure analysis unambiguously identifies an intrinsic contribution to the AMR: the energy band crossing depends on the magnetization direction with spin-orbit coupling. The predicted properties of the AMR in $\text{Co}_x\text{Fe}_{1-x}$ alloys, including its dependence on the current orientation and alloy concentration, are well confirmed by our transport experiments on single-crystal samples. The simultaneously measured longitudinal and transverse resistivities in the experiment exhibit a reciprocal relationship along high-symmetry crystal axes, which is reproduced by a phenomenological model.

The work at Fudan University was supported by the National Key Research and Development Program of China (Grant No. 2016YFA0300703), National Natural Science Foundation of China (Grant No. 11974079 and No. 11734006), and the Program of Shanghai Academic Research Leader (No. 17XD1400400). The work at Beijing Normal University was supported by the National Natural Science Foundation of China (Grant No. 61774018 and No. 11734004), the Recruitment Program of Global Youth Experts, and the Fundamental Research Funds for the Central Universities (Grant No. 2018EYT03). The work at Argonne was supported by the U.S. Department of Energy (DOE), Office of Science, Materials Science and Engineering Division. The work at OU was supported by the U.S. National Science Foundation under Grant No. DMR-1808892.

* These authors contributed equally.

† wuyizheng@fudan.edu.cn

‡ zyuan@bnu.edu.cn

- [1] C. Chappert, A. Fert, F. N. Van Dau, The emergence of spin electronics in data storage. *Nat. Mater.* **6**, 813 (2007).
- [2] W. Döring, Die Abhängigkeit des Widerstandes von Nickelkristallen von der Richtung der spontanen Magnetisierung. *Ann. Phys. (Leipzig)* **424**, 259–276 (1938).
- [3] T. McGuire, R. Potter, Anisotropic magnetoresistance in ferromagnetic 3d alloys. *IEEE Trans. Magn.* **11**, 1018–1038 (1975).
- [4] L. Berger, Influence of Spin-Orbit Interaction on the Transport Processes in Ferromagnetic Nickel Alloys, in the Presence of a Degeneracy of the 3d Band. *J. Appl. Phys.* **34**, 1360–1361 (1963).
- [5] I. Campbell, A. Fert, O. Jaoul, The spontaneous resistivity anisotropy in Ni-based alloys. *J. Phys. C: Solid State Phys.* **3**, S95 (1970).
- [6] N. Nagaosa, J. Sinova, S. Onoda, A. H. MacDonald, N. P. Ong, Anomalous Hall effect. *Rev. Mod. Phys.* **82**, 1539 (2010).
- [7] J. Sinova, S. O. Valenzuela, J. Wunderlich, C. H. Back, T. Jungwirth, Spin Hall effect. *Rev. Mod. Phys.* **87**, 1213 (2015).
- [8] Di Xiao, Ming-Che Chang, and Qian Niu, Berry phase effects on electronic properties. *Rev. Mod. Phys.* **82**, 1959 (2010).
- [9] Y. Bason, J. Hoffman, C. Ahn, L. Klein, Magnetoresistance tensor of $\text{La}_{0.8}\text{Sr}_{0.2}\text{MnO}_3$. *Phys. Rev. B* **79**, 092406 (2009).
- [10] W. Limmer, M. Glunk, J. Daeubler, T. Hummel, W. Schoch, R. Sauer, C. Bihler, H. Huebl, M. Brandt, S. Goennenwein, Angle-dependent magnetotransport in cubic and tetragonal ferromagnets: Application to (001)- and (113)A-oriented (Ga, Mn)As. *Phys. Rev. B* **74**, 205205 (2006).
- [11] W. Limmer, J. Daeubler, L. Dreher, M. Glunk, W. Schoch, S. Schwaiger, R. Sauer, Advanced resistivity model for arbitrary magnetization orientation applied to a series of compressive-to tensile-strained (Ga, Mn)As layers. *Phys. Rev. B* **77**, 205210 (2008).
- [12] N. Naftalis, A. Kaplan, M. Schultz, C. Vaz, J. Moyer, C. Ahn, L. Klein, Field-dependent anisotropic magnetoresistance and planar Hall effect in epitaxial magnetite thin films. *Phys. Rev. B* **84**, 094441 (2011).
- [13] Z. Ding, J. X. Li, J. Zhu, T. P. Ma, C. Won, Y. Z. Wu, Three-dimensional mapping of the anisotropic magnetoresistance in Fe_3O_4 single crystal thin films. *J. Appl. Phys.* **113**, 17B103 (2013).
- [14] M. Tondra, D. K. Lottis, K. Riggs, Y. Chen, E. D. Dahlberg, G. Prinz, Thickness dependence of the anisotropic magnetoresistance in epitaxial iron films. *J. Appl. Phys.* **73**, 6393–6395 (1993).
- [15] R. Van Gorkom, J. Caro, T. Klapwijk, S. Radelaar, Temperature and angular dependence of the anisotropic magnetoresistance in epitaxial Fe films. *Phys. Rev. B* **63**, 134432 (2001).
- [16] T. Hupfauer, A. Matos-Abiad, M. Gmitra, F. Schiller, J. Loher, D. Bougeard, C. H. Back, J. Fabian, D. Weiss, Emergence of spin-orbit fields in magnetotransport of quasi-two-dimensional iron on gallium arsenide. *Nat. Commun.* **6**, 7374 (2015).
- [17] X. Xiao, J. H. Liang, B. L. Chen, J. X. Li, D. H. Ma, Z. Ding, Y. Z. Wu, Current-direction dependence of the transport properties in single-crystalline face-centered-cubic cobalt films. *J. Appl. Phys.* **118**, 043908 (2015).
- [18] X. Xiao, J. X. Li, Z. Ding, Y. Z. Wu, Four-fold symmetric anisotropic magnetoresistance of single-crystalline Ni (001) film. *J. Appl. Phys.* **118**, 203905 (2015).
- [19] H. Nakayama, M. Althammer, Y. -T. Chen, K. Uchida, Y. Kajiwara, D. Kikuchi, T. Ohtani, S. Geprägs, M. Opel, S. Takahashi, R. Gross, G. E. W. Bauer, S. T. Goennenwein, E. Saitoh, Spin Hall magnetoresistance induced by a nonequilibrium proximity effect. *Phys. Rev. Lett.* **110**, 206601 (2013).
- [20] H. Nakayama, Y. Kanno, H. An, T. Tashiro, S. Haku, A. Nomura, K. Ando, Rashba-Edelstein Magnetoresistance in Metallic Heterostructures. *Phys. Rev. Lett.* **117**, 116602 (2016).
- [21] L. Zhou, H. Song, K. Liu, Z. Luan, P. Wang, L. Sun, S. Jiang, H. Xiang, Y. Chen, J. Du, H. Ding, K. Xia, J. Xiao, D. Wu, Observation of spin-orbit magnetoresistance in metallic thin films on magnetic insulators. *Sci. Adv.* **4**, eaao3318 (2018).
- [22] M. Trushin, K. Výborný, P. Moraczewski, A. A. Kovalev, J. Schliemann, and T. Jungwirth, Anisotropic magnetoresistance of spin-orbit coupled carriers scattered from polarized magnetic impurities. *Phys. Rev. B* **80**, 134405 (2009).
- [23] M. A. Schoen, D. Thonig, M. L. Schneider, T. Silva, H. T. Nembach, O. Eriksson, O. Karis, J. M. Shaw, Ultra-low magnetic damping of a metallic ferromagnet. *Nat.*

- Phys. **12**, 839 (2016).
- [24] A. J. Lee, J. T. Brangham, Y. Cheng, S. P. White, W. T. Ruane, B. D. Esser, D. W. McComb, P. C. Hammel, F. Yang, Metallic ferromagnetic films with magnetic damping under 1.4×10^{-3} . Nat. Commun. **8**, 234 (2017).
 - [25] Y. Li, F. L. Zeng, S. S. L. Zhang, H. Shin, H. Saglam, V. Karakas, O. Ozatay, J. E. Pearson, O. Heinonen, Y. Z. Wu, A. Hoffmann, W. Zhang, Giant Anisotropy of Gilbert Damping in Epitaxial CoFe Films. Phys. Rev. Lett. **122**, 117203 (2019).
 - [26] A. A. Starikov, Y. Liu, Z. Yuan, P. J. Kelly, Calculating the transport properties of magnetic materials from first principles including thermal and alloy disorder, non-collinearity, and spin-orbit coupling. Phys. Rev. B **97**, 214415 (2018).
 - [27] See Supplemental Materials at [URL], which includes Refs. [45–53], for computational details, characterization of the samples and AMR measurement, and additional analysis based on band structure and the phenomenological theory.
 - [28] I. Turek, V. Drchal, J. Kudrnovský, M. Sob, P. Weinberger, *Electronic structure of disordered alloys, surfaces and interfaces*. (Kluwer, Boston-London-Dordrecht, 1997).
 - [29] S.-Y. Yang, H. Yang, E. Derunova, S. S. Parkin, B. Yan, M. N. Ali, Symmetry demanded topological nodal-line materials. Advances in Physics: X **3**, 1414631 (2018).
 - [30] S. Syzranov, B. Skinner, Electron transport in nodal-line semimetals. Phys. Rev. B **96**, 161105 (2017).
 - [31] B. Sbierski, G. Pohl, E. J. Bergholtz, P. W. Brouwer, Quantum transport of disordered Weyl semimetals at the nodal point. Phys. Rev. Lett. **113**, 026602 (2014).
 - [32] S. Das Sarma, S. Adam, E. Hwang, E. Rossi, Electronic transport in two-dimensional graphene. Rev. Mod. Phys. **83**, 407 (2011).
 - [33] Q. -D. Jiang, H. Jiang, H. Liu, Q.-F. Sun, X.-C. Xie, Topological Imbert-Fedorov shift in Weyl semimetals. Phys. Rev. Lett. **115**, 156602 (2015).
 - [34] Q. -D. Jiang, H. Jiang, H. Liu, Q.-F. Sun, X. C. Xie, Chiral wave-packet scattering in Weyl semimetals. Phys. Rev. B **93**, 195165 (2016).
 - [35] L. Šmejkal, Y. Mokrousov, B. Yan, A. H. MacDonald, Topological antiferromagnetic spintronics. Nat. Phys. **14**, 242 (2018).
 - [36] S. Y. Bodnar, L. Šmejkal, I. Turek, T. Jungwirth, O. Gomonay, J. Sinova, A. Sapozhnik, H.-J. Elmers, M. Kläui, M. Jourdan, Writing and reading antiferromagnetic Mn₂Au by Néel spin-orbit torques and large anisotropic magnetoresistance. Nat. Commun. **9**, 348 (2018).
 - [37] K. Gilmore, M. D. Stiles, J. Seib, D. Steiauf, and M. Fähnle, Anisotropic damping of the magnetization dynamics in Ni, Co, and Fe. Phys. Rev. B **81**, 174414 (2010).
 - [38] H. Ebert, S. Mankovsky, D. Ködderitzsch, P. J. Kelly, Ab initio calculation of the Gilbert damping parameter via the linear response formalism. Phys. Rev. Lett. **107**, 066603 (2011).
 - [39] Z. Yuan, K. M. D. Hals, Y. Liu, A. A. Starikov, A. Brataas, P. J. Kelly, Gilbert damping in noncollinear ferromagnets. Phys. Rev. Lett. **113**, 266603 (2014).
 - [40] D. Thonig, O. Eriksson, and M. Pereiro, Magnetic moment of inertia within the torque-torque correlation model. Sci. Rep. **7**, 931 (2017).
 - [41] U. Bajpai and B. K. Nikolić, Time-retarded damping and magnetic inertia in the Landau-Lifshitz-Gilbert equation self-consistently coupled to electronic time-dependent nonequilibrium Green functions. Phys. Rev. B **99**, 134409 (2019).
 - [42] V. Kamberský, On ferromagnetic resonance damping in metals. Czech. J. Phys. **26**, 1366 (1976).
 - [43] B. Raquet, M. Viret, E. Sondergard, O. Cespedes, R. Mamy, Electron-magnon scattering and magnetic resistivity in 3d ferromagnets. Phys. Rev. B **66**, 024433 (2002).
 - [44] R. R. Birss, *Symmetry and magnetism*. (North-Holland Amsterdam, 1964).
 - [45] P. Khomyakov, G. Brocks, V. Karpan, M. Zwierzycki, and P. J. Kelly, Conductance calculations for quantum wires and interfaces: Mode matching and Green's functions. Phys. Rev. B **72**, 035450 (2005).
 - [46] I. Turek, J. Kudrnovsk, and V. Drchal, Ab initio theory of galvanomagnetic phenomena in ferromagnetic metals and disordered alloys. Phys. Rev. B **86**, 014405 (2012).
 - [47] A. A. Starikov, P. J. Kelly, A. Brataas, Y. Tserkovnyak, and G. E. W. Bauer, Unified first-principles study of Gilbert damping, spin-flip diffusion, and resistivity in transition metal alloys. Phys. Rev. Lett. **105**, 236601 (2010).
 - [48] O. Gunnarsson, Band model for magnetism of transition metals in the spin-density-functional formalism. J. Phys. F: Metal Phys. **6**, 587 (1976).
 - [49] Z. Yuan and P. J. Kelly, Spin-orbit-coupling induced torque in ballistic domain walls: Equivalence of charge-pumping and nonequilibrium magnetization formalisms. Phys. Rev. B **93**, 224415 (2016).
 - [50] Y. Su, X. S. Wang and X. R. Wang, A generic phase between disordered Weyl semimetal and diffusive metal. Sci. Rep. **7**, 14382 (2017).
 - [51] G. Prinz, Stabilization of bcc Co via epitaxial growth on GaAs. Phys. Rev. Lett. **54**, 1051 (1985).
 - [52] W. N. Cao, J. Li, G. Chen, J. Zhu, C. R. Hu, Y. Z. Wu, Temperature-dependent magnetic anisotropies in epitaxial Fe/CoO/MgO (001) system studied by the planar Hall effect. Appl. Phys. Lett. **98**, 262506 (2011).
 - [53] F. L. Zeng, C. Zhou, M. W. Jia, D. Shi, Y. Huo, W. Zhang, Y. Z. Wu, Strong current-direction dependence of anisotropic magnetoresistance in single crystalline Fe/GaAs(110) films, J. Magn. Magn. Mater. **499**, 166204 (2020).